Charged particle identification using the liquid Xenon calorimeter of the CMD-3 detector

V.L. Ivanov, G.V. Fedotovich, A.V. Anisenkov, A.A. Grebenuk, A.A. Kozyrev, A.A. Ruban, K. Yu. Mikhailov
Budker Institute of Nuclear Physics (Novosibirsk, Russia)
CMD-3 collaboration
e-mail: vyacheslav_lvovich_ivanov@mail.ru

Abstract

This report describes a currently being developed procedure of the charged particle identification for CMD-3 detector, installed at the VEPP-2000 collider. The procedure is based on the application of the boosted decision trees classification method, and uses as input variables, among others, the specific energy losses of charged particle in the layers of the liquid Xenon calorimeter. The efficiency of the procedure is demonstrated by an example of the extraction of events of $e^+e^- \to K^+K^-(\gamma)$ process in the center of mass energy range from 1.28 to 1.65 GeV.

1. LXe calorimeter of the CMD-3 detector

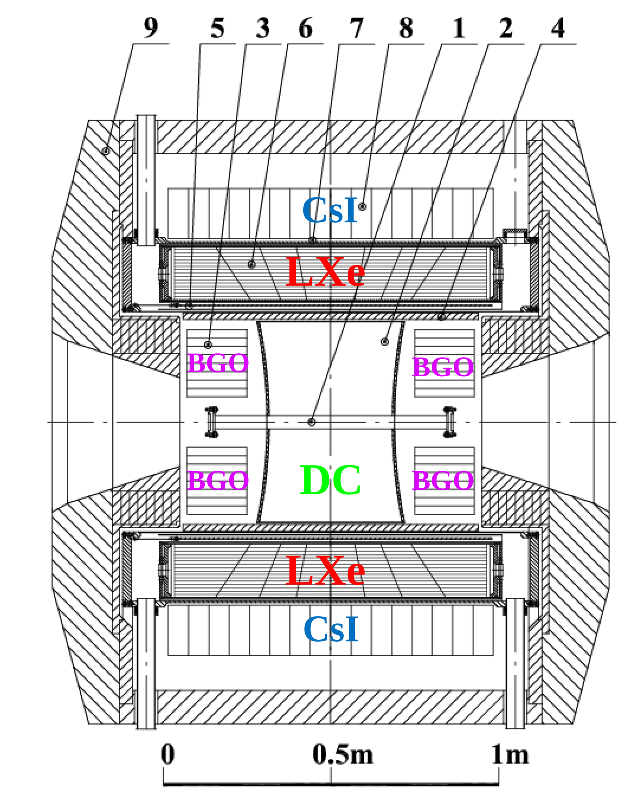

Figure 1. The CMD-3 detector layout: 1 - beam pipe, 2 - drift chamber, 3 - BGO endcap calorimeter, 4 - Z-chamber, 5 - superconducting solenoid, 6 - LXe calorimeter, 7 - time-of-flight system, 8 - CsI calorimeter, 9 – yoke.

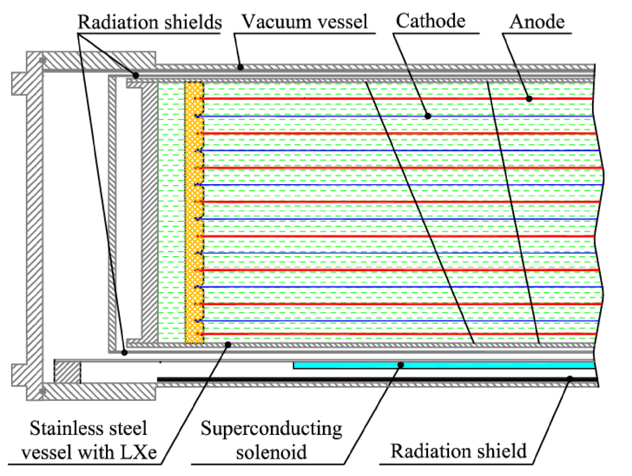

Figure 2. LXe calorimeter electrodes structure.

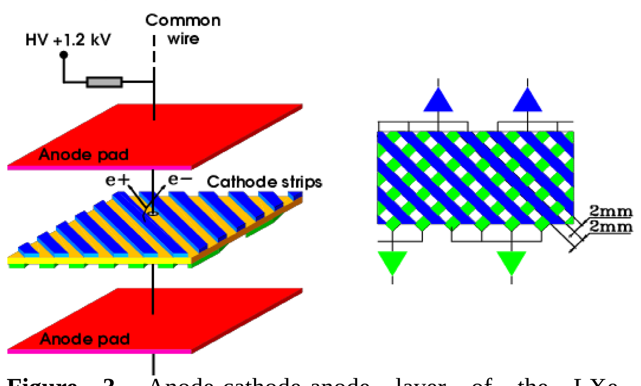

Figure 3. Anode-cathode-anode layer of the LXe calorimeter. A strip structure of cathode is shown.

- The tracking system of CMD-3 detector consists of the cylindrical drift chamber (DC) and double-layer cylindrical multiwire proportional Z-chamber, installed inside a superconducting solenoid with 1.0-1.3 T magnetic field (see Fig. 1). Amplitude information from the DC wires is used to measure the specific ionization losses dE/dx_{DC} of charged particles.
- The liquid Xenon (LXe) calorimeter of 5.4 X_0 thickness consists of 14 cylindrical ionization chambers formed by 7 cylindrical cathodes and 8 anodes with 10.2 mm gap between them (see Fig. 2). Cathodes are divided into 2112 strips to provide precise coordinate measurement along with the measurement of the specific energy losses (dE/dx_{LXe}) in each of 14 anode-cathode layers (see Fig. 3). Each side of the cathode cylinder contains about 150 strips. The strips on the opposite sides of cathode are mutually perpendicular, which allows one to measure z and φ coordinates of the "hit" in the strips channels.

2. dE/dx_{LXe} vs. dE/dx_{DC}: general considerations

- In this report we will focus on the charged kaons identification. The separation of the single kaons from pions/muons using only dE/dx_{DC} can be reliably performed only for the particles momenta lower than 450 MeV/c (see Fig. 4). For the K^+K^-, $K^+K^-\pi^0$, $K^+K^-2\pi^0$, $K_SK^\pm\pi^\mp$ final states at high c.m. energies it is hard or impossible to obtain sufficiently pure sample of signal events using only dE/dx_{DC} and the energy-momentum conservation. Hence the dE/dx_{LXe} -based PID should be used.
- Distributions of the dE/dx_{LXe} in seven LXe double layers depending on the particle momentum for the simulated single e^-, μ^-, π^-, K^- are shown in Figs. 5-6. These are the major dE/dx_{DC-LXe} differences:

1. dE/dx_{LXe} increases (on average) layer by layer because of the particle deceleration (see Fig. 7);
2. For the $\mu^\pm$, $\pi^\pm$, $K^\pm$ and $p^\pm$ there are different momentum thresholds p_{thr} of the particle absorption in the material in front of the calorimeter p_{thr}, below which only the products of particle decay or of the absorption by nucleon can reach the calorimeter. For kaons $p^K{}_{thr}$ is ~400 MeV/c (see Fig. 5);
3. The values of the p_{thr}, as well as the distributions of the dE/dx_{LXe}, depend on the expected distance of the pass d_{LXe} of the particle in the LXe-layer, because the shower profile (for $e^\pm$), the probability of nuclear interaction (for hadrons) and the particle's deceleration rate are the functions of d_{LXe}.
4. In contrast with the DC the probability of nuclear interaction hadrons in LXe is not small (~25%). The accuracy of simulation of such interactions is not guaranteed and requires verification.

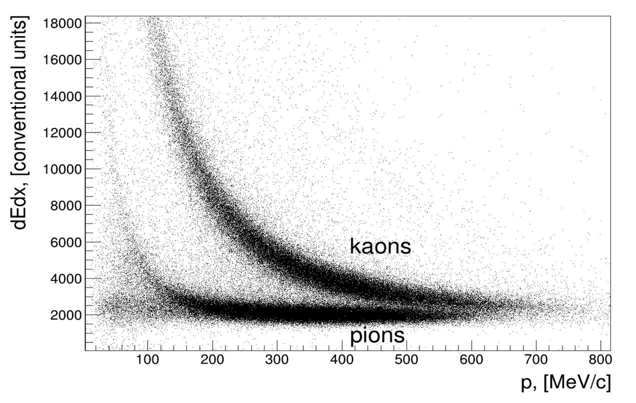

Figure 4. The dE/dx_{DC} vs. particle momentum distribution for the events of the process $K^+K^-\pi^+\pi^-$, selected in the simulation, $\sqrt{s} \in (1.5\text{ GeV}; 2.0\text{ GeV})$.

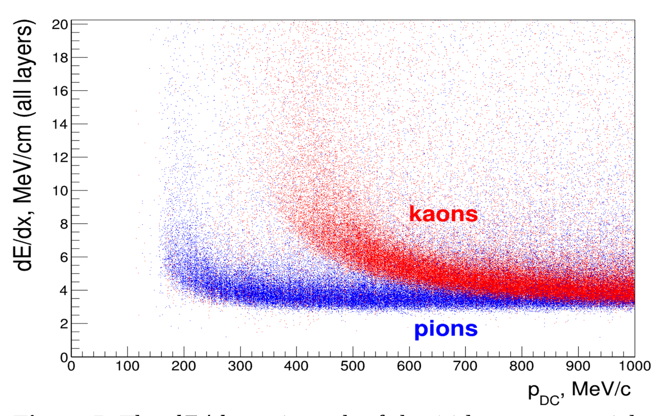

Figure 5. The dE/dx_{LXe} in each of the 14 layers vs. particle momentum for the simulated $K^\pm$ and $\pi^\pm$.

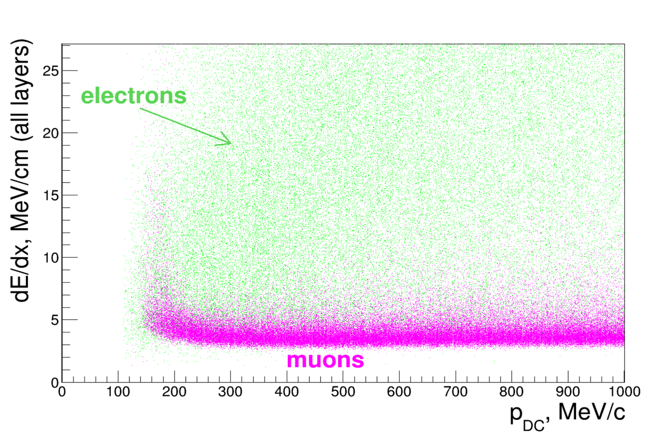

Figure 6. The dE/dx_{LXe} in each of the 14 layers vs. particle momentum for the simulated $\mu^\pm$ and $e^\pm$.

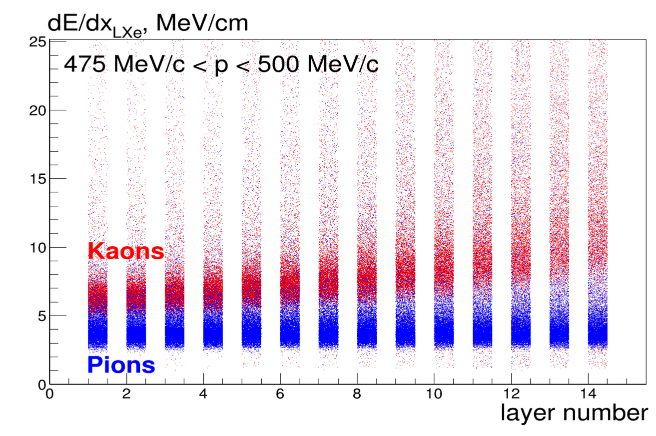

Figure 7. The dE/dx_{LXe} in 14 layers for the simulated $K^\pm$ and $\pi^\pm$ with the momenta in range from 0.475 to 0.5 GeV/c.

3. General idea of the charged PID procedure

The idea of the LXe-based PID is the following:

- For each DC-track with curvature, small enough to hit the particle in LXe, we calculate 10 values of the responses (R) of the multivariate classifiers (taken from TMVA package), trained for the optimal separation of particular pairs of particles in the particular momentum p and d_{LXe} parameter ranges δp_i and $\delta d_{LXe,j}$ (see table below and Fig. 8).
- For the training of the classifiers we simulate ~$5 \cdot 10^6$ events with single $e^\pm$, $\mu^\pm$, $\pi^\pm$, $K^\pm$, $p^\pm$, having the momentum and d_{LXe} parameter uniformly distributed in the ranges from 0.04 GeV to 1.1 GeV and from 1.0 to 1.5 correspondingly. In total we have 4400 classifiers to be trained with the 14 values of dE/dx_{LXe} as the input variables.

	$e^\pm$	$\mu^\pm$	$\pi^\pm$	$K^\pm$
$\mu^\pm$	$R_{i,j}(\mu^\pm/e^\pm)$	-	-	-
$\pi^\pm$	$R_{i,j}(\pi^\pm/e^\pm)$	$R_{i,j}(\pi^\pm/\mu^\pm)$	-	-
$K^\pm$	$R_{i,j}(K^\pm/e^\pm)$	$R_{i,j}(K^\pm/\mu^\pm)$	$R_{i,j}(K^\pm/\pi^\pm)$	-
$p^\pm$	$R_{i,j}(p^\pm/e^\pm)$	$R_{i,j}(p^\pm/\mu^\pm)$	$R_{i,j}(p^\pm/\pi^\pm)$	$R_{i,j}(p^\pm/K^\pm)$

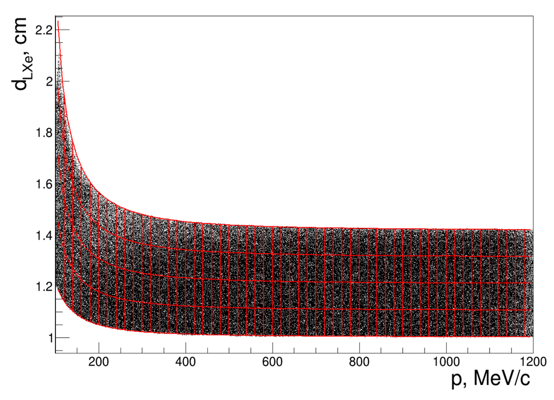

Figure 8. The distribution of the particle momenta vs. d_{LXe} for simulated μ^+ (training sample). The limits of $\delta p_i : \delta d_{LXe,j}$ cells, inside which particular classifiers are trained are also shown.

4. Selection of the best classifier

- First of all one should choose the most powerful classifier from about 40 classification methods, proposed by the TMVA package. We tested different methods for the task of K/π separation at $p = 870$ MeV/c, see Fig. 9. We found BDT (boosted decision trees) to be the globally most powerful method.

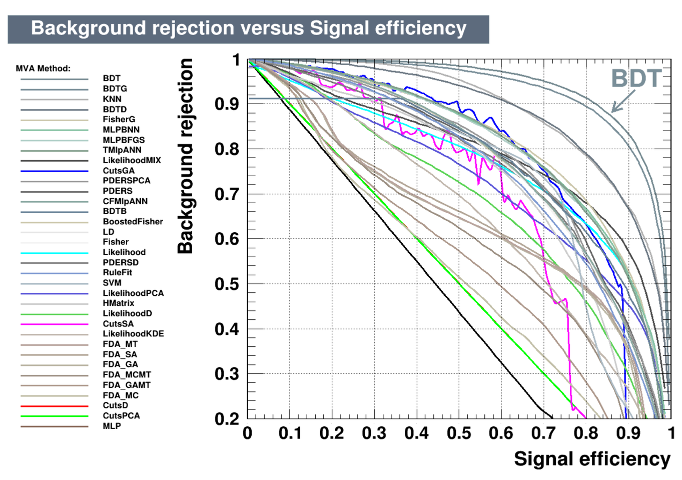

Figure 9. The dependence of the background rejection efficiency on the signal selection efficiency for K/π separation at the momenta 870 MeV/c for different classification methods trained and tested.

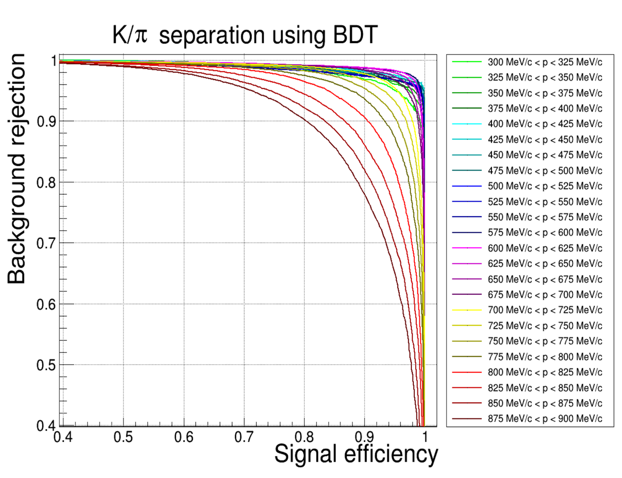

Figure 10. The dependence of the BDT background rejection efficiency on the signal selection efficiency for the K/π separation in the different momentum ranges from 300 to 900 MeV/c.

5. Detector response tuning

- Since the simulated samples of $e^\pm$, $\mu^\pm$, $\pi^\pm$, $K^\pm$, $p^\pm$ are used for BDT training, the correctness of the simulation should be verified. The comparison of dE/dx_{LXe} spectra for cosmics in the experiment and simulation is shown in Fig. 11 (after the strips calibration). One can see, that experimental spectra are wider, than simulated. The reason for that is, presumably, the complex structure of the cathode strips, see Fig. 3. The charge, induced (in simulation) on the strip by the ionization element, is calculated in the approximation of the charge between two infinite conductive planes, i.e. complex cathode structure is neglected.
- The influence of the ionization in the upper (lower) cathode-anode layer on the strips in lower (upper) layer in simulation is described by special parameter – transparency coefficient $T_{l=1..7}$, specific for each layer.
- To obtain the values of transparency we reproduced the geometry of 7 anode-cathode-anode layers in the CST electromagnetic processes simulation package. We put the uniformly charged brick (with a dielectric permittivity as that of the liquid xenon and with the transverse dimensions equal to the period of cathode structure) in the cathode-anode gap. We simulate the electric field distribution and calculate T_l as a ratio of the total charges, induced on the lower and upper strips. The obtained with 5% precision transparency values are T_1=0.290, T_2=0.239, T_3=0.371, T_4=0.353, T_5=0.397, T_6=0.365, T_7=0.357. Their correctness can be demonstrated by the good agreement of the inclination of bands in the $dE/dx^{up}{}_{LXe} : dE/dx^{down}{}_{LXe}$ distributions in simulation and experiment, see Fig. 14.
- Further it will be convenient for us to use the half-sum and half-difference of the "decorrelated" dE/dx_{LXe}, measured by the upper and lower strips.
- The major simulation-experiment difference (for cosmics) is manifested in the broadening of the dE/dx_{diff} spectra, see Fig. 14. Our hypothesis is that the reason is in the *redistribution* of induced charge between strips, caused by the anticorrelated variation of the transparency coefficient around the average values, obtained from CST. We account for the broadening in dE/dx_{diff} by introducing additional Gaussian noise, see Fig. 15, and use some (much smaller) noise to fit the dE/dx_{summ} spectra, Fig. 16.
- Finally, we can check the agreement of the dE/dx_{summ} and dE/dx_{diff} spectra for pions from the $e^+e^- \to 2\pi^+2\pi^-$ process, see Figs. 17-18. We see the agreement, good enough for MC-based BDT training.

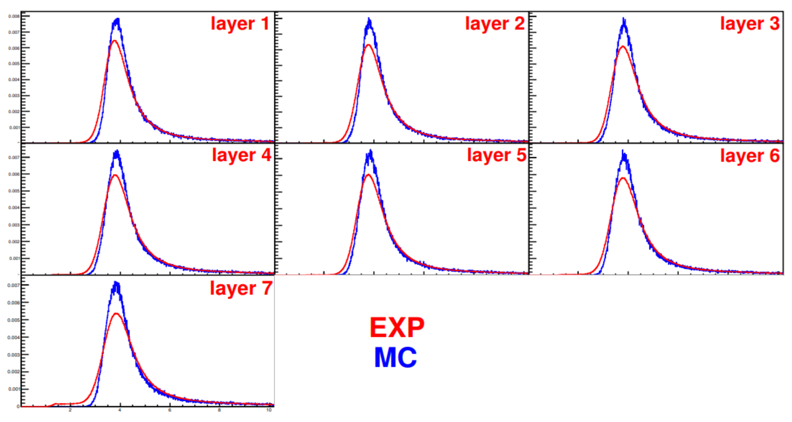

Figure 11. The comparison of the dE/dx_{LXe} spectra for cosmics after the strips calibration.

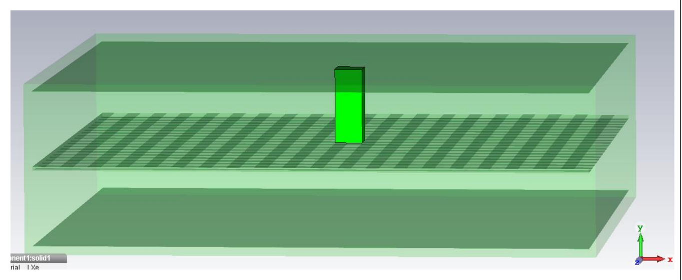
Figure 12. The uniformly charged brick in the anode-cathode gap. The model is used for the transparency coefficients calculation.

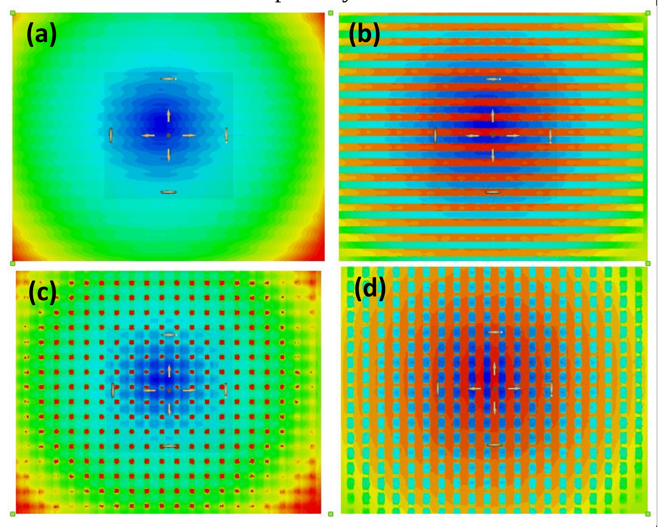

Figure 13. The distributions of the y-component of the D-field above the upper strips (a), under upper strips (b), above the lower strips (c), under lower strips (d).

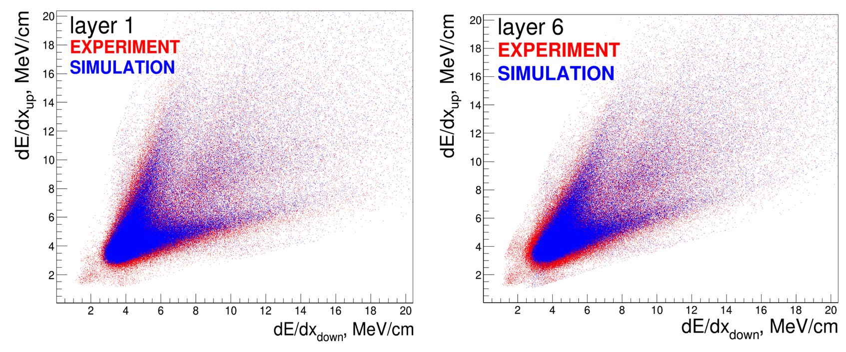

Figure 14. The $dE/dx^{up}{}_{LXe} : dE/dx^{down}{}_{LXe}$ distributions in the 1st and 6th layers.

$$\begin{bmatrix} (dE/dx)^{\mathrm{meas}}_{\mathrm{up}} \\ (dE/dx)^{\mathrm{meas}}_{\mathrm{low}} \end{bmatrix} = \frac{1}{1+T_l} \begin{bmatrix} 1 & T_l \\ T_l & 1 \end{bmatrix} \cdot \begin{bmatrix} (dE/dx)^{\mathrm{real}}_{\mathrm{up}} \\ (dE/dx)^{\mathrm{real}}_{\mathrm{low}} \end{bmatrix}$$

$$\begin{bmatrix} (dE/dx)_{\mathrm{summ}} \\ (dE/dx)_{\mathrm{diff}} \end{bmatrix} = \frac{1}{2(1-T_l)} \begin{bmatrix} 1 & 1 \\ 1 & -1 \end{bmatrix} \cdot \begin{bmatrix} 1 & -T_l \\ -T_l & 1 \end{bmatrix} \cdot \begin{bmatrix} (dE/dx)^{\mathrm{meas}}_{\mathrm{up}} \\ (dE/dx)^{\mathrm{meas}}_{\mathrm{low}} \end{bmatrix}$$

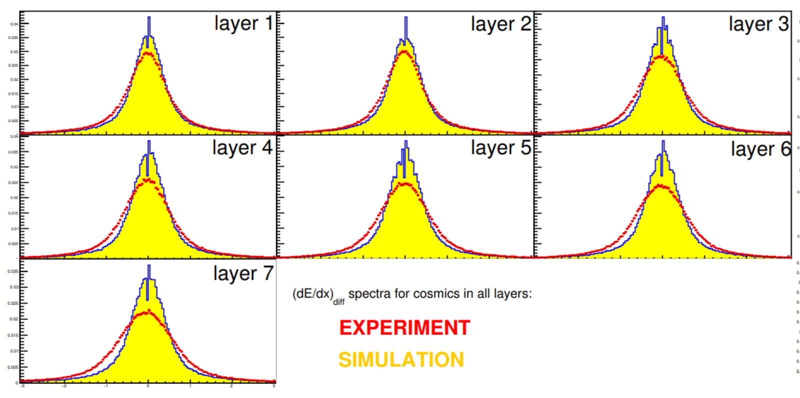

Figure 14. The dE/dx_{diff} distributions in 7 layers for cosmics (before tuning).

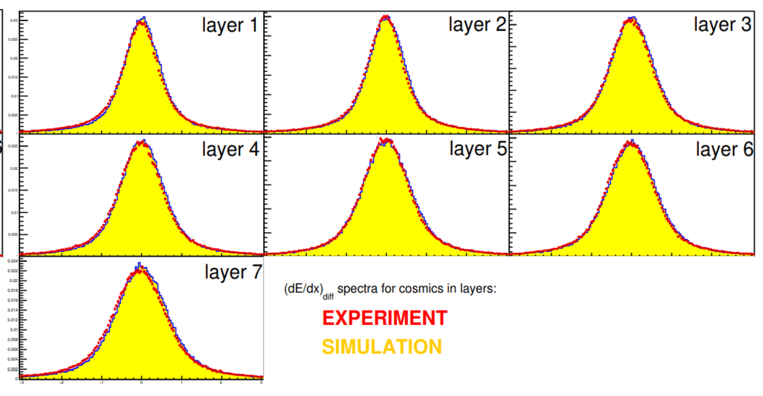

Figure 15. The dE/dx_{diff} distributions in 7 layers for cosmics (after tuning).

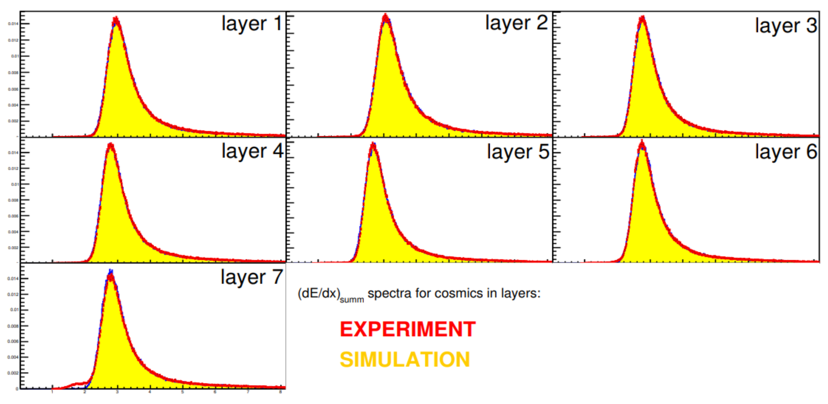

Figure 16. The dE/dx_{summ} distributions in 7 layers for cosmics (after tuning).

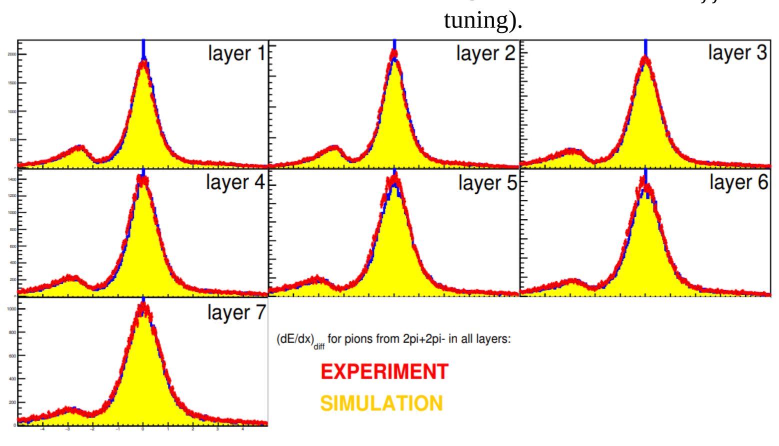

Figure 17. The dE/dx_{diff} distributions in 7 layers for pions from $2\pi^+2\pi^-$ (after tuning).

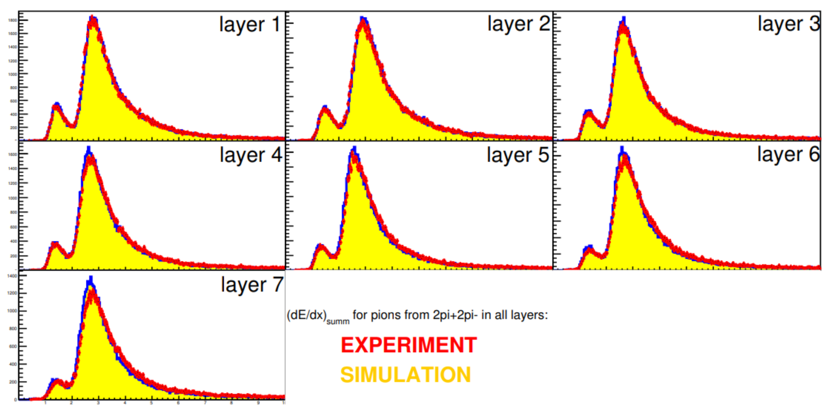

Figure 18. The dE/dx_{summ} distributions in 7 layers for pions from $2\pi^+2\pi^-$ (after tuning).

6. Example: selection of $e^+e^- \to K^+K^-(\gamma)$ events for $\sqrt{s} \in (1.28\text{ GeV}; 1.65\text{ GeV})$

- We illustrate the efficiency of the developed PID technique by an example of selection of the events of $e^+e^- \to K^+K^-(\gamma)$ process in the c.m. energy range from 1.28 to 1.65 GeV on the basis of 12.5 pb^{-1} of integrated luminosity. We use the simulation of the events of signal and the major background processes ($e^+e^- \to \pi^+\pi^-$, $\mu^+\mu^-$, e^+e^- and cosmics).
- We select the events having two oppositely charged DC-tracks with polar angles $\theta_{DC}{}^{1,2} \in (0.9; \pi - 0.9)$, satisfying the condition of collinearity in $r - \varphi$ plane: $||\varphi_{DC}{}^1 - \varphi_{DC}{}^2| - \pi| < 0.15$.
- The distribution of the averaged energy deposition of two charged particles in the calorimeter vs. the energy disbalance $\Delta E = \sqrt{\vec{p}_{K^+}{}^2 + m_K{}^2} + \sqrt{\vec{p}_{K^-}{}^2 + m_K{}^2} + |p_{z,K^+} + p_{z,K^-}| - 2E_{beam}$ in the experiment and simulation is shown in Figure 19. The term $|p_{z,K^+} + p_{z,K^-}|$ is added to ΔE to compensate the energy of ISR photons, emitted along beam axis. In addition to the clusters of K^+K^-, $\pi^+\pi^-$, $\mu^+\mu^-$, e^+e^- final states the horizontal band of cosmic muons is seen.
- Further, Fig. 22a-b show the distributions of the $(BDT_{K^+/e^+} + BDT_{K^-/e^-})/2$ parameter ($\sqrt{s}$=1.282 and 1.65 GeV correspondingly). The shown cuts are used to suppress e^+e^- final state, see the result in Fig. 20.
- Then we apply the cut on $(BDT_{K^+/\mu^+} + BDT_{K^-/\mu^-})/2$ to suppress cosmics, $\mu^+\mu^-$ and $\pi^+\pi^-$ final states, see Fig. 23a-b. As a result we obtain almost pure sample $e^+e^- \to K^+K^-(\gamma)$ events, see Fig. 21.
- Finally, using the selected K^+K^- events, we can prove the correctness of the dE/dx_{LXe} simulation for kaons, see Figs. 24-25.

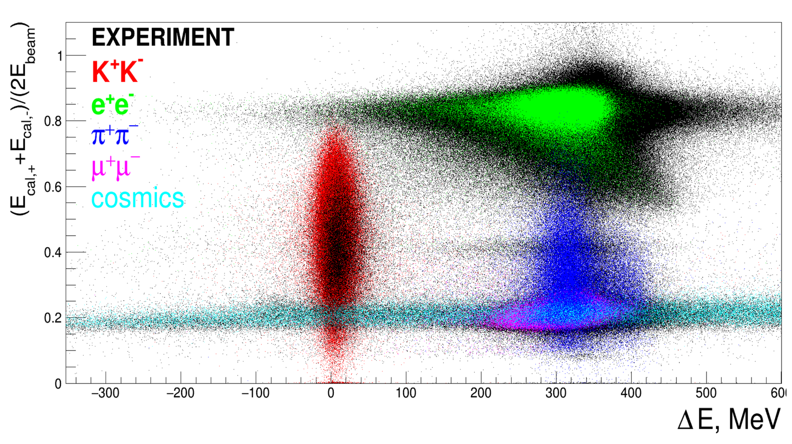

Figure 19. The distribution of the averaged energy deposition of two charged particles in the calorimeter vs. the energy disbalance ΔE for the selected events. All energy points are combined.

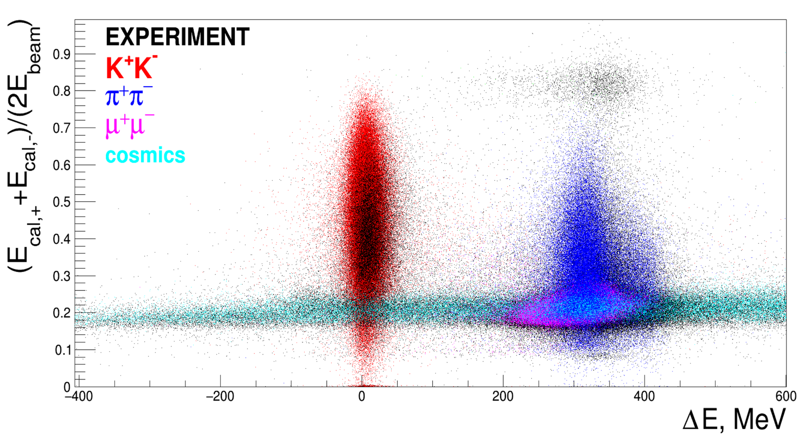

Figure 20. The distribution of the averaged energy deposition of two charged particles in the calorimeter vs. the energy disbalance ΔE for the selected events after e^+e^- suppression. All energy points are combined.

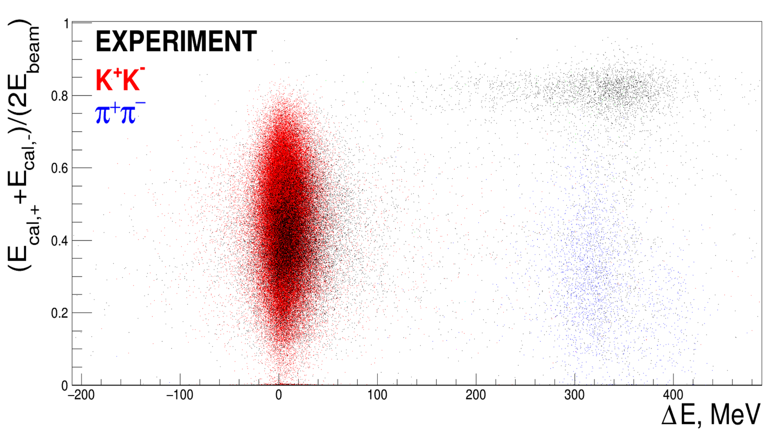

Figure 21. The distribution of the averaged energy deposition of two charged particles in the calorimeter vs. the energy disbalance ΔE for the selected events after e^+e^-, $\mu^+\mu^-$, $\pi^+\pi^-$ and cosmics suppression. All energy points are combined.

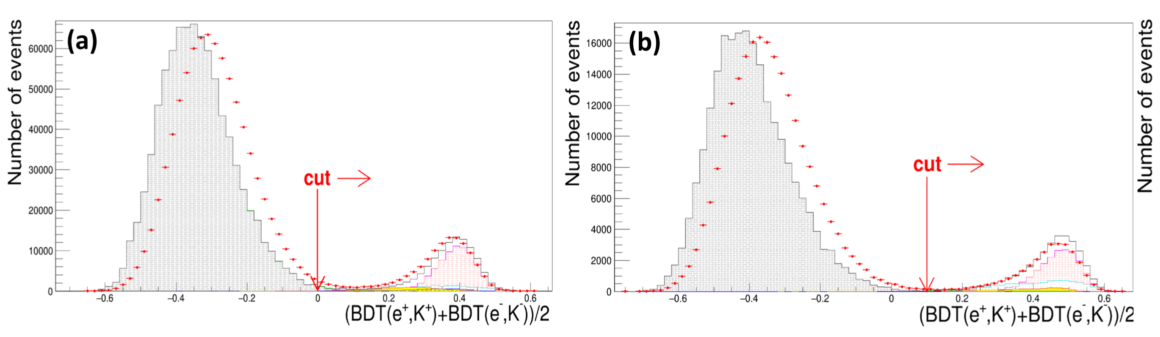

Figure 22. The distributions of the $(BDT_{K^+/e^+} + BDT_{K^-/e^-})/2$ parameter (a - $\sqrt{s}$=1.282 GeV, b – 1.65 GeV) in the experiment (red markers), simulation of e^+e^- (gray), $\mu^+\mu^-$ (magenta), $\pi^+\pi^-$ (turquoise), K^+K^- (yellow).

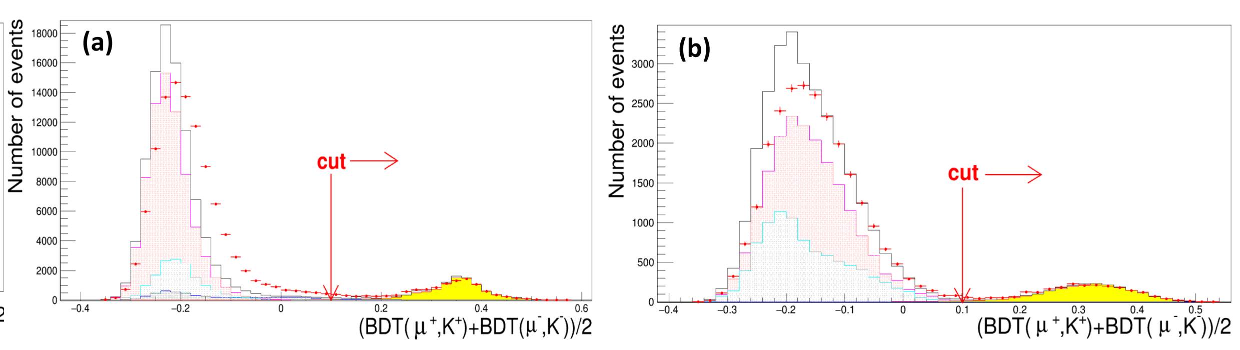

Figure 23. The distributions of the $(BDT_{K^+/\mu^+} + BDT_{K^-/\mu^-})/2$ parameter (a - $\sqrt{s}$=1.282 GeV, b – 1.65 GeV) in the experiment (red markers), simulation of e^+e^- (gray), $\mu^+\mu^-$ (magenta), $\pi^+\pi^-$ (turquoise), K^+K^- (yellow).

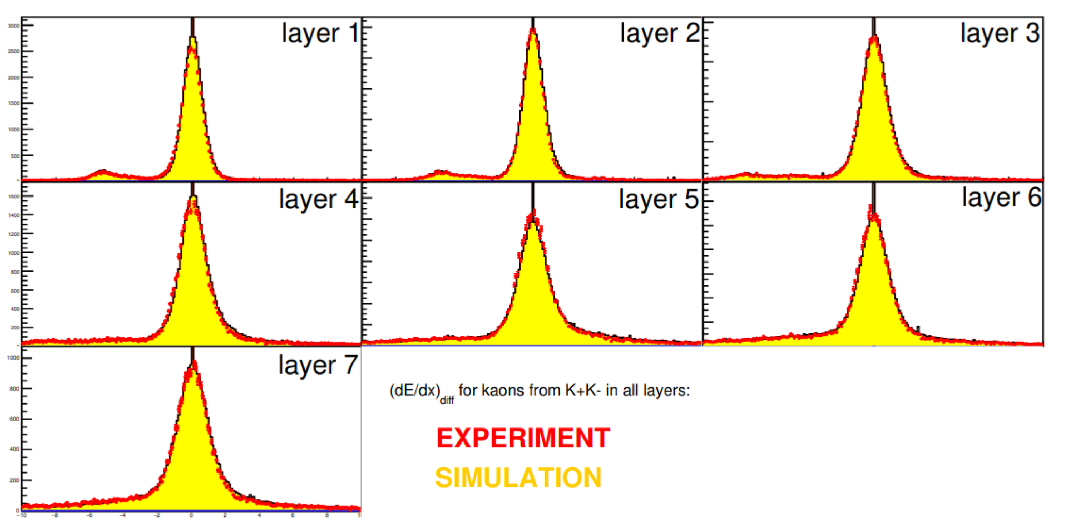

Figure 24. The dE/dx_{diff} distributions in 7 layers for kaons from K^+K^- final state (after tuning).

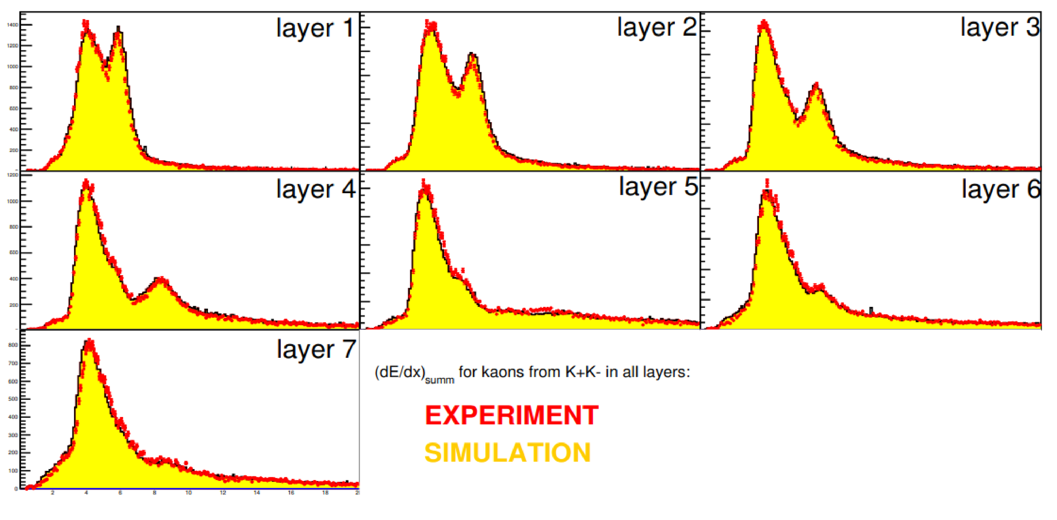

Figure 25. The dE/dx_{summ} distributions in 7 layers for kaons from K^+K^- final state (after tuning).

7. Plans

- We have no problems in the detector response simulation for m.i.p.s, but see some simulation-experiment discrepancy for showers. Presumably, it is caused by the correlated/anticorrelated variation of the transparency coefficient in the lower and upper layer. We plan to study these variations thoroughly using CST-simulation.
- We plan to apply the described technique to the data collected in the runs of 2017-2018 and to use it in the analyzes of the final states K^+K^-, $K^+K^-\pi^0$, $K^+K^-2\pi^0$, $K_SK^\pm\pi^\mp$.

10th International Workshop on Ring Imaging Cherenkov Detectors, 29 July – 4 August 2018, Russian Academy of Sciences, Moscow